Published OnlineFirst May 20, 2015; DOI: 10.1158/1078-0432.CCR-14-2018

Cancer Therapy: Preclinical

Clinical Cancer Research

Model Matters: Differences in Orthotopic Rat Hepatocellular Carcinoma Physiology Determine Therapy Response to Sorafenib

Claudia Groß[1], Katja Steiger[2], Sufyan Sayyed[1], Irina Heid[1], Annette Feuchtinger[5], Axel Walch[5], Julia Heß[6], Kristian Unger[6], Horst Zitzelsberger[6], Marcus Settles[1], Anna Melissa Schlitter[2], Juliane Dworniczak[1], Jennifer Altomonte[3], Oliver Ebert[3], Markus Schwaiger[4], Ernst Rummeny[1], Andreas Steingötter[7], Irene Esposito[2,8], and Rickmer Braren[1]

Abstract

Purpose: Preclinical model systems should faithfully reflect the complexity of the human pathology. In hepatocellular carcinoma (HCC), the tumor vasculature is of particular interest in diagnosis and therapy. By comparing two commonly applied preclinical model systems, diethylnitrosamine induced (DEN) and orthotopically implanted (McA) rat HCC, we aimed to measure tumor biology noninvasively and identify differences between the models.

Experimental Design: DEN and McA tumor development was monitored by MRI and PET. A slice-based correlation of imaging and histopathology was performed. Array CGH analyses were applied to determine genetic heterogeneity. Therapy response to sorafenib was tested in DEN and McA tumors.

Results: Histologically and biochemically confirmed liver damage resulted in increased ^{18}F-fluorodeoxyglucose (FDG) PET uptake and perfusion in DEN animals only. DEN tumors exhibited G1–3 grading compared with uniform G3 grading of McA tumors. Array comparative genomic hybridization revealed a highly variable chromosomal aberration pattern in DEN tumors. Heterogeneity of DEN tumors was reflected in more variable imaging parameter values. DEN tumors exhibited lower mean growth rates and FDG uptake and higher diffusion and perfusion values compared with McA tumors. To test the significance of these differences, the multikinase inhibitor sorafenib was administered, resulting in reduced volume growth kinetics and perfusion in the DEN group only.

Conclusions: This work depicts the feasibility and importance of in depth preclinical tumor model characterization and suggests the DEN model as a promising model system of multifocal nodular HCC in future therapy studies. *Clin Cancer Res; 21(19); 4440–50. ©2015 AACR.*

See related commentary by Weber et al., p. 4254

Introduction

Hepatocellular carcinoma (HCC) presents the most common primary liver tumor and third most common cause of cancer-related death worldwide (1). Tumor angiogenesis is required for HCC development, enabling the distinction of dysplastic and tumor nodules by contrast enhanced imaging (2) and providing the rationale for antiangiogenic therapy of advanced-stage disease, for example, with the receptor tyrosine kinase inhibitor sorafenib and transarterial chemoembolization (TACE; ref. 3). Unsatisfactory preclinical modeling of HCC and the lack of robust tools for the assessment of treatment response beyond the evaluation of tumor burden (4) have hampered progress in testing and validating new tumor therapies (5).

Preclinical HCC model systems, in particular genetically engineered mouse models (GEMMS), have been invaluable tools for the molecular dissection of human hepatocarcinogenesis to date (6). However, translational research requires model systems that recapitulate the human condition in its complexity. For example, lack of an underlying liver damage, a frequent accompanying condition in human HCC, presents an important shortcoming of several preclinical model systems (7). As a consequence preclinical therapy trials conducted on aberrantly, for example, subcutaneously located tumors, showing outstanding drug efficacy, failed to translate into clinical efficacy most likely due to a nonphysiologic simplicity of the model system with clonal origin of the tumor, lack of tumor matrix, an insufficient subcutaneous blood supply, and sometimes lack of a functioning immune response (8, 9). Considering the clinical significance of TACE treatment in advanced-stage HCC, model systems should furthermore provide the possibility for combinatorial treatment testing,

[1]Institut für Radiologie, [2]Institut für Pathologie, [3]II. Medizinische Klinik, [4]Nuklearmedizinische Klinik, Klinikum Rechts der Isar, Technische Universität München, Munich, Germany. [5]Institut für Pathologie und [6]Abteilung für Strahlenzytogenetik, Helmholtz-Zentrum München, Neuherberg, Germany. [7]Abteilung für Gastroenterologie und Hepatologie, Universität Zürich, Zurich, Switzerland. [8]Institut für Pathologie, Medizinische Universität Innsbruck, Innsbruck, Austria.

Note: Supplementary data for this article are available at Clinical Cancer Research Online (http://clincancerres.aacrjournals.org/).

C. Groß, K. Steiger, and S. Sayyed contributed equally to this article.

Corresponding Author: Rickmer Braren, Institute of Diagnostic and Interventional Radiology, Klinikum Rechts der Isar, Technische Universität München, Ismaninger Street 22, 81675 Munich. Phone: 49-89-4140-2626; Fax: 49-89-4140-6653; E-mail: rbraren@tum.de

doi: 10.1158/1078-0432.CCR-14-2018

Published OnlineFirst May 20, 2015; DOI: 10.1158/1078-0432.CCR-14-2018

Translational Relevance

Preclinical model systems applied in translational research should faithfully represent the human pathology, and preclinical therapy studies should adhere to the same rigorous trial design applied in human. We performed multiparametric multimodal imaging to identify differences in two common rat HCC model systems, diethylnitrosamine induced (DEN) and orthotopically implanted (McA) rat HCC. In contrast with the McA model, DEN tumors exhibited a high level of inter - and intratumoral heterogeneity. In addition, major differences in tumor growth kinetics, tumor composition, and perfusion were identified and confirmed by quantitative histopathologic analyses. Interestingly, DEN tumors only showed response to sorafenib treatment. We believe these findings are of high translational relevance as they indicate important differences between model systems and in addition support the rat DEN model for the future testing of novel combinatorial therapy regimen.

for example, testing of combinations of TACE and targeted therapies, which is technically difficult to achieve in mouse models. The diethylnitrosamine (DEN)-induced rat HCC model system was first introduced in the early 1960s, exhibiting multifocal HCC in a chronically damaged liver background. In contrast, the multifocal orthotopical implantation model is a frequently used alternative, where tumors develop within a healthy liver after portal vein injection of tumor cells.

Quantitative assessment of HCC physiology and therapy response is challenging, both *in vivo* and *ex vivo*. MRI and PET have been successfully applied for the noninvasive measurement of unifocally implanted orthotopic rat tumors and therapy response (10). The aim of this study was to further implement a multimodal multiparametric imaging platform in the more complex multifocal McA and DEN rat HCC model systems and to compare quantitative imaging, histologic, and genetic data for potential differences in liver and tumor physiology.

Materials and Methods

Animal models and imaging protocol

All animal experiments were approved and performed in accordance with the institutional animal care and use committee's guidelines and the government of Bavaria, Germany. As depicted in Supplementary Fig. S1A, chemically induced tumors (DEN) were established in 24 seven-week-old male Wistar rats (Charles River Laboratories) by oral feeding of 0.01% DEN (Sigma) dissolved in drinking water for a period of 8 weeks. Orthotopically implanted multifocal HCC (McA) was generated in 7 six-week-old Buffalo rats (Harlan) by portal vein infusion of 10^7 syngeneic McA-RH7777 cells (ATCC) as a 1 mL suspension of serum-free DMEM as previously described (11). MRI was performed using a 1.5 Tesla clinical MRI system (Achieva 1.5T, Philips Healthcare) with a standard human ovoid, split-case wrist coil (SENSE Wrist coil 4 elements, Philips Healthcare) as previously described (10). After an incubation period of 12 days (McA) or 8 weeks (DEN), longitudinal T_2-weighted (T2w) turbo spin-echo imaging (slice thickness = 0.7 mm, in-plane resolution = 0.5×0.5 mm^2, TR/TE = 3170 ms/90 ms, NSA = 8) was performed on day 12, 19, 22, 26, and 28 (McA) or weekly (6–8 days interval; DEN) for tumor detection and volumetric analysis. Once tumors reached a size $\geq$5 mm in diameter additional DCE-MRI and DWI experiments were performed as previously described (3, 10). For PET imaging animals were examined with a dedicated μPET-CT (Inveon, Siemens). Animals were fasted 4 hours before PET imaging. Static image acquisition was performed 45 minutes after injection of 5 to 10 MBq 18F-fluorodeoxyglucose (FDG) or 18F-fluorothymidine (FLT) via a tail vein catheter (Tacq = 15 minutes). During imaging, animals were maintained under isoflurane anesthesia (3% isoflurane, 1.5% oxygen, Abbott GmbH) and monitored by continuous recording of the ECG and rectal temperature (SA Instruments Inc.).

Sorafenib therapy

In a second cohort, 23 DEN-induced and 7 orthotopically implanted animals bearing tumor nodules $\geq$5 mm were treated with the multikinase inhibitor sorafenib (Nexavar, Bayer) or vehicle every other day (0.1 mg/kg redissolved in DMSO, i.p.). Tumor response was monitored longitudinally by T2w-, DCE- and DWI-MRI on day −1, 0, 1, 7, and 14 (Supplementary Fig. S1B). After final imaging, rats were kept under anesthesia and euthanized. Tumors were processed for histologic analyses.

Data analysis and statistics

Tumor volume (V) was manually segmented and calculated from the T_2w datasets (Osirix; http://www.osirix.com). The paired and unpaired *t* test and tumor growth kinetics estimation were performed using Prism GraphPad 4. DCE-MRI and DWI data were analyzed using in-house software written in IDL (ITT VIS) as previously described (10) DCE-MRI data were analyzed semi-quantitatively by calculating tumor-to-muscle and liver-to-muscle ratios of the area under the Gd-DTPA concentration time curves of the first 60 seconds (AUGC60) after contrast agent injection. 3D volumes of interest (VOI) of fused PET–MRI images were analyzed using the absolute mean value of the tumor 3D VOI and normalized to two 2D spinal muscle ROIs to calculate the mean tumor-to-muscle and liver-to-muscle ratios.

Serum biochemistry

Before euthanization, blood samples were collected from the tail vein and centrifuged at 3,000 rpm for 20 minutes at 4°C. After centrifugation, serum samples were separated and stored at −20°C until further use. The marker enzymes of liver damage, aspartate aminotransferase (ASAT) alanine aminotransferase (12), cholinesterase (ChE), and gamma-glutamyl transpeptidase (GGT) were analyzed in serum samples of all rats (Diasys) following the manufacturer's instructions.

Histopathology and immunohistochemistry

Immediately after final imaging animals were sacrificed under deep anesthesia. Perfusion fixation was performed using 20 mL PBS to flush out all blood from the vasculature, followed by manual infusion of 200 mL 1% PFA. Thereafter, the livers were removed and emerged for 48 hours in 4% PFA, briefly washed, transferred to 70% ethanol and embedded in paraffin before hematoxylin and eosin (H&E) staining. Immunohistochemistry of tumor and liver tissue was performed using the Ventana Discovery (Roche) autostainer. Antibodies with respective dilutions are listed in a separate table (Supplementary Table S1). Tumors were classified with respect to histotype and graded as per

Published OnlineFirst May 20, 2015; DOI: 10.1158/1078-0432.CCR-14-2018

WHO criteria for human and rat HCC (13, 14). All lesions were qualitatively categorized and graded for arbitrary score 1 to 3. For further H&E and CD31 analyses, all slides were scanned at ×10 objective magnification by an Olympus BX51 scanner with an xy pixel resolution of 0.6466 × 0.6466 μm (Olympus dotSlide System, Fa. Olympus) and ×20 objective magnification by a Mirax scanner with an xy pixel resolution of 0.328 × 0.328 μm (Fa. Carl Zeiss, Mirax Desk). For each of the resulting digital slides, subsets were extracted from areas of tumor and analyzed using commercially available software (Definiens Enterprise Image Intelligence Suite, Fa. Definiens AG). For Ki-67 staining analysis, 10 to 15 nonoverlapping high-power field images were captured from different regions of each tumor at ×40 magnification (light microscope PrimoStar, Fa. Carl Zeiss). The captured images were analyzed using software (Axio Vision Rel 4.8, Zeiss). Threshold for all nuclei and Ki-67 positive nuclei was defined manually for each section based on the staining intensity. Total number of Ki-67–positive nuclei and number of total nuclei present were counted per image and the ratio of Ki-67 positive to total nuclei was calculated. CD3-, CD45RA, and CD163 immunohistochemistry was evaluated semiquantitatively by counting the numbers of positive cells per low power field (light microscope olympus BX53, objective ×20, field number 22). For human HCC tumor vessel staining, CD34 antibody was used (clone QBEnd/10, 1:100) on seven formalin-fixed, paraffin-embedded human HCC specimens obtained from the archives of the Institute of Pathology of the Technical University of Munich (Supplementary Table S2). Calculation of vessel lumen area was performed as described above. For necrosis quantification tumors were H&E stained and analyzed using Definiens software (Definiens Developer XD 64, tissue studio). The use of tissue was approved by the local ethics committees and written informed consent was obtained from the patients before resection.

Array CGH sample preparation and hybridization

To perform array CGH analysis, histologic formalin-fixed paraffin-embedded tissue sections from livers with HCCs mounted on glass slides were macrodissected for enrichment of tumor cells based on the assessment of an H&E stained reference slide. After deparaffinisation with xylene, the tissue was scratched off the slide into the lysis buffer provided by the Qiagen DNeasy FFPE Kit (Fa. Qiagen). Genomic DNA was extracted and purified according to the manufacturer's protocol followed by quantification with the Nanodrop spectrophotometer. The DNA from 4 to 5 strain-specific healthy livers was pooled and used as reference DNA. For each array, 250 ng of reference DNA was labeled with Cy5, and the same amount of sample DNA was labeled with Cy3 using an oligo array CGH labeling kit (Enzo). The labeled DNA was purified using Microcon YM-50 columns (Millipore) and hybridized on custom designed whole genome rat CGH 8 × 60 k arrays (Agilent) according to the manufacturer's protocol.

Array CGH data analysis and visualization

After washing and scanning according to the manufacturer's protocol the resulting data text files were subjected to preprocessing, normalization, and copy-number calling within the statistical platform R (www.R-project.org). Spatial normalization was conducted using the Bioconductor package MANOR (15) and the copy-number status of each array probe was called using the CGHcall package (16) followed by complexity reduction using the CGHregions package (17).

To visually assess the copy-number profiles, karyogram-like plots were generated along rat ideogrammes using an in-house written function. PCA plots based on the probe-wise probability values for normal copy numbers were generated using the ggbiplot package (https://github.com/vqv/ggbiplot) to visually assess global differences copy-number profiles. The copy-number status of the *Flt1* (*Vegfr*) and *Vegfa* genes were visualized using the level plot function from the lattice package (http://cran.r-project.org/web/packages/lattice/index.html).

Comparability of genomic copy-number changes detected in our animal model with that occurring in human cryptogenic HCC as published in a study by Schlaeger and colleagues (18), we conducted a synteny analysis between rat and human as described in Wolf and colleagues (19). The analysis was visualized using functions from the CRAN package RCircos. Array CGH data have been deposited at the ArrayExpress repository (accession number: E-MTAB-3507).

Results

Liver damage in the DEN model

Histopathologically nontumorous liver tissue showed increased fibrosis in DEN compared with McA animals (Fig. 1A and B), indicative of tissue remodeling. Furthermore, bile duct hyperplasia and increased numbers of mitotic figures were noted as signs of chronic toxic tissue damage and hepatocellular regeneration in DEN compared with McA animals (Fig. 1C and D). In addition, cytoplasmic vacuolization and fatty change of hepatocytes, multiple clear cell and basophilic foci of cellular alteration (FCA) and intralobular tissue macrophage infiltration (Supplementary Fig. S2A) reflected chronic liver damage of DEN-treated animals. In contrast, the architecture of McA liver tissue was unchanged and showed a normal sinusoidal structure without matrix deposition (Fig. 1B and D). Liver function as determined by serum enzyme levels was altered with aspartate aminotransferase (ASAT) and alanine aminotransferase (12) levels significantly elevated before tumor development, beginning at 4 weeks and further increasing at 8 weeks of DEN treatment, indicating hepatocellular dysfunction (Fig. 1E and F). Endpoint GGT serum levels were not significantly changed (Fig. 1G). The cholinesterase (ChE), a marker of liver synthesis, was reduced in both models (Fig. 1H).

The histopathologic changes in nontumorous liver tissue resulted in higher perfusion and (AUGC60 liver-to-muscle ratio: 6.34 ± 1.50 and 3.84 ± 1.84, $P < 0.005$) and glucose metabolism (FDG liver-to-muscle ratio: 3.33 ± 0.47 and 2.38 ± 0.28; $P < 0.001$) in nontumorous liver tissue of DEN compared with McA animals.

Detection and longitudinal monitoring of tumor development in the DEN and McA model

Both models showed 100% tumor penetrance (Supplementary Table S3). Histopathologically and immunohistochemically, all DEN tumors were characterized as HCC-expressing hepatocyte-specific antigen (Hep Par-1, data not shown) with different degrees of differentiation (G1 to G3 grading pattern; Fig. 2A) and variable extracapsular penetration, closely resembling human HCC. Most DEN tumors revealed prominent trabecular growth consisting of large cells with intracytoplasmic fat droplets and eosinophilic inclusions. In addition, dense G3, acinar-papillary G2 tumors as well as pseudoglandular HCC with central or scattered hemorrhagic degeneration were present underlining the

Published OnlineFirst May 20, 2015; DOI: 10.1158/1078-0432.CCR-14-2018

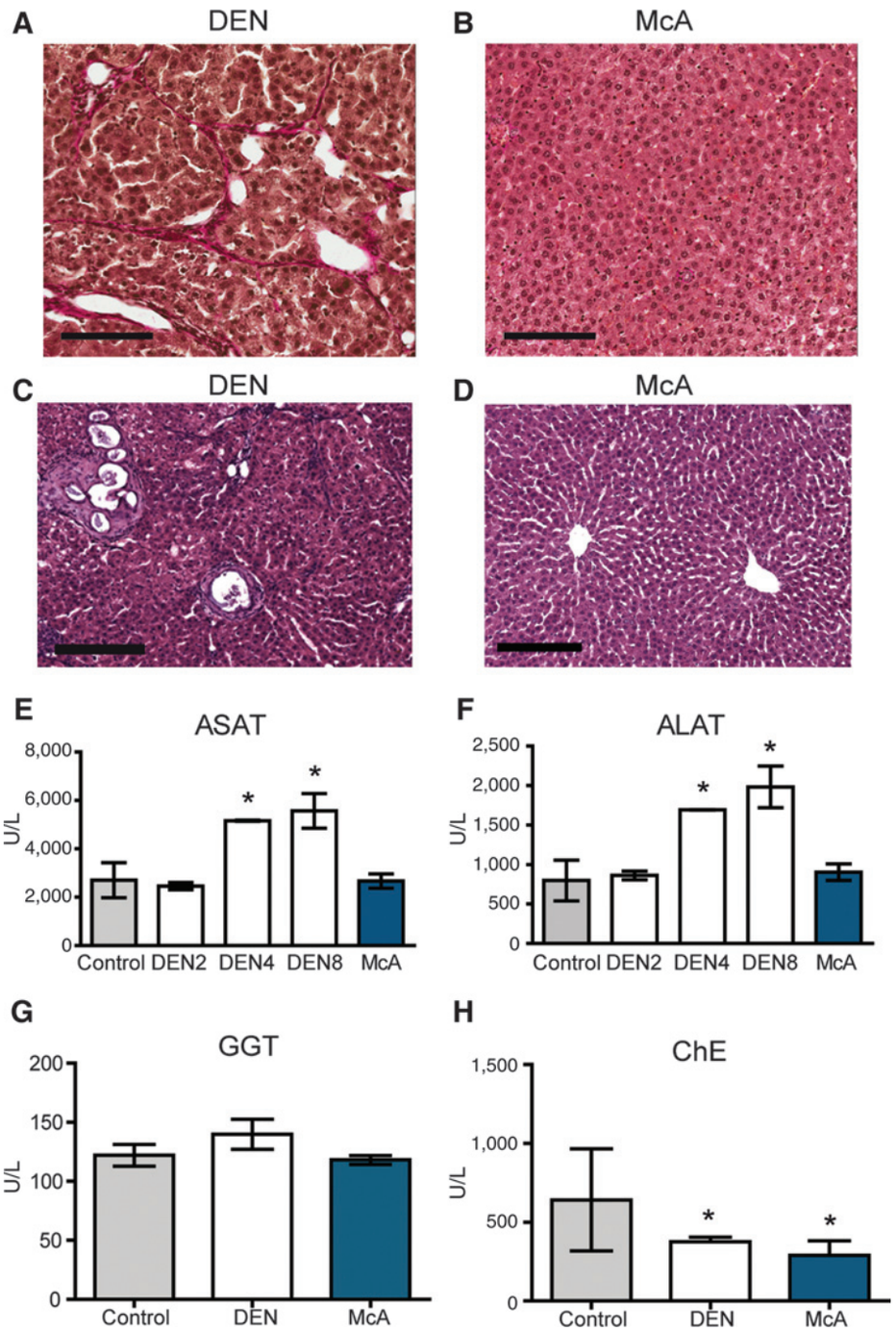

Figure 1.
Liver damage in DEN fed animals. A and B, Elastica van Gieson staining shows collagen fibers (red) in DEN livers only. C and D, H&E staining reveals distorted sinusoidal architecture and fibrotic septations (left) compared with the normal architecture in transplanted animals; scale bars, 100 μm. E and F, ASAT and ALAT serum levels gradually increase in DEN treated animals from 4 to 8 weeks after onset of DEN feeding. G and H, DEN and McA animals exhibit no change in GGT and reduced ChE serum levels.

wide spectrum of DEN-induced rat HCC histology. In contrast, McA tumors revealed a uniformly dense G3 grading pattern with trabecular growth. A higher number of tumor-infiltrating $CD3^+$ lymphocytes in DEN induced tumors reflect human HCC, whereas an increased peritumoral lymphocytic infiltration in McA tumors is a model-specific response (Supplementary Fig. S2B). In HCC of both models, only single intra- and peritumoral $CD45RA^+$ lymphocytes and neutrophil granulocytes were observed (data not shown).

Tumors were reliably identified on T2w images by their hyperintense appearance compared with surrounding nontumorous liver tissue. Tumor signal intensity was again more heterogeneous in DEN tumors. The heterogeneous grading pattern was reflected in a more variable and often slower onset of tumor growth of DEN compared with McA detected by longitudinal T2w imaging (Fig. 2B). The mean doubling-time was 0.52 ± 0.20 days versus 2.0 ± 1.83 days in DEN and McA, respectively. Histologically, the observed differences in volume growth kinetics correlated well

Published OnlineFirst May 20, 2015; DOI: 10.1158/1078-0432.CCR-14-2018

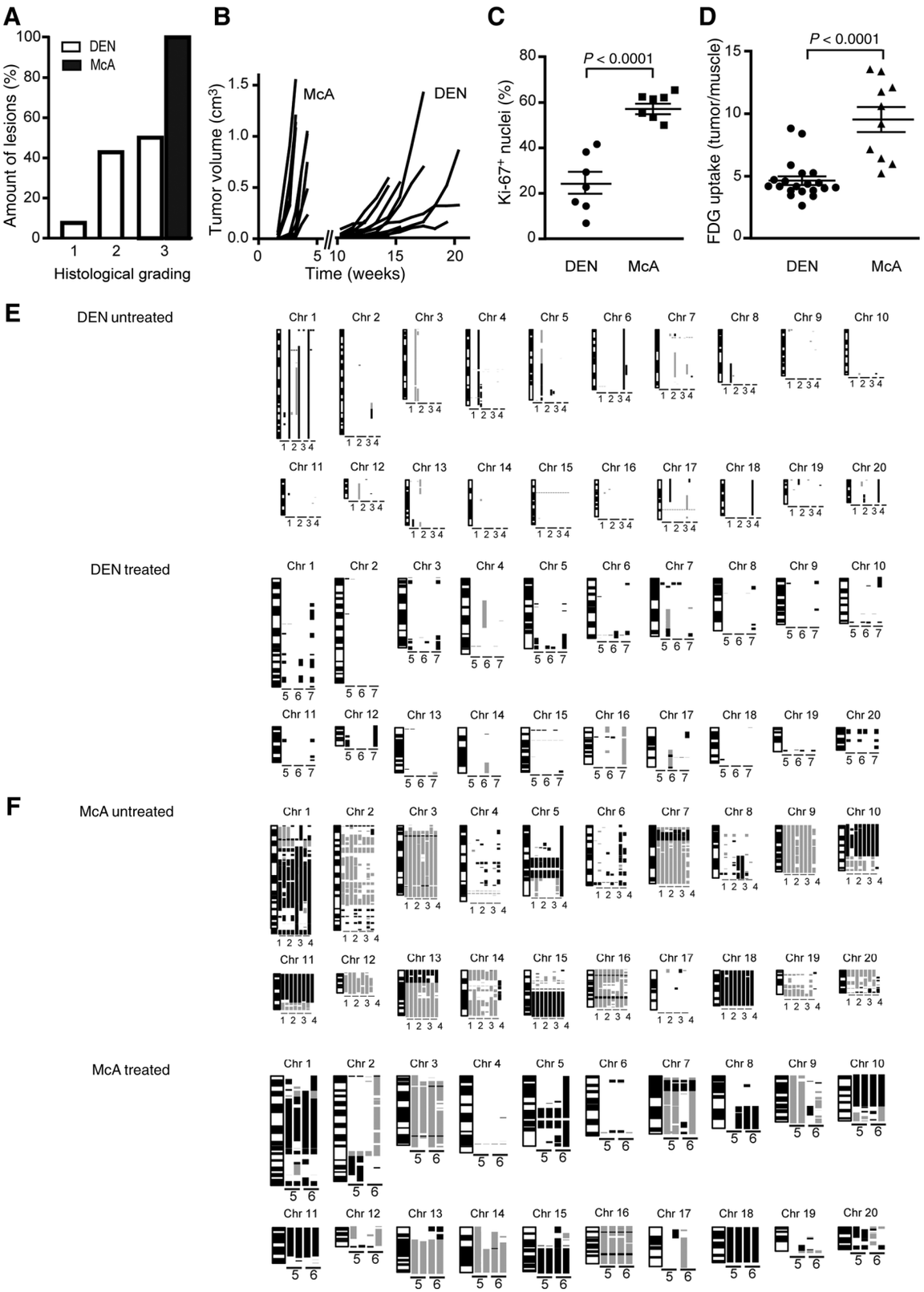

Published OnlineFirst May 20, 2015; DOI: 10.1158/1078-0432.CCR-14-2018

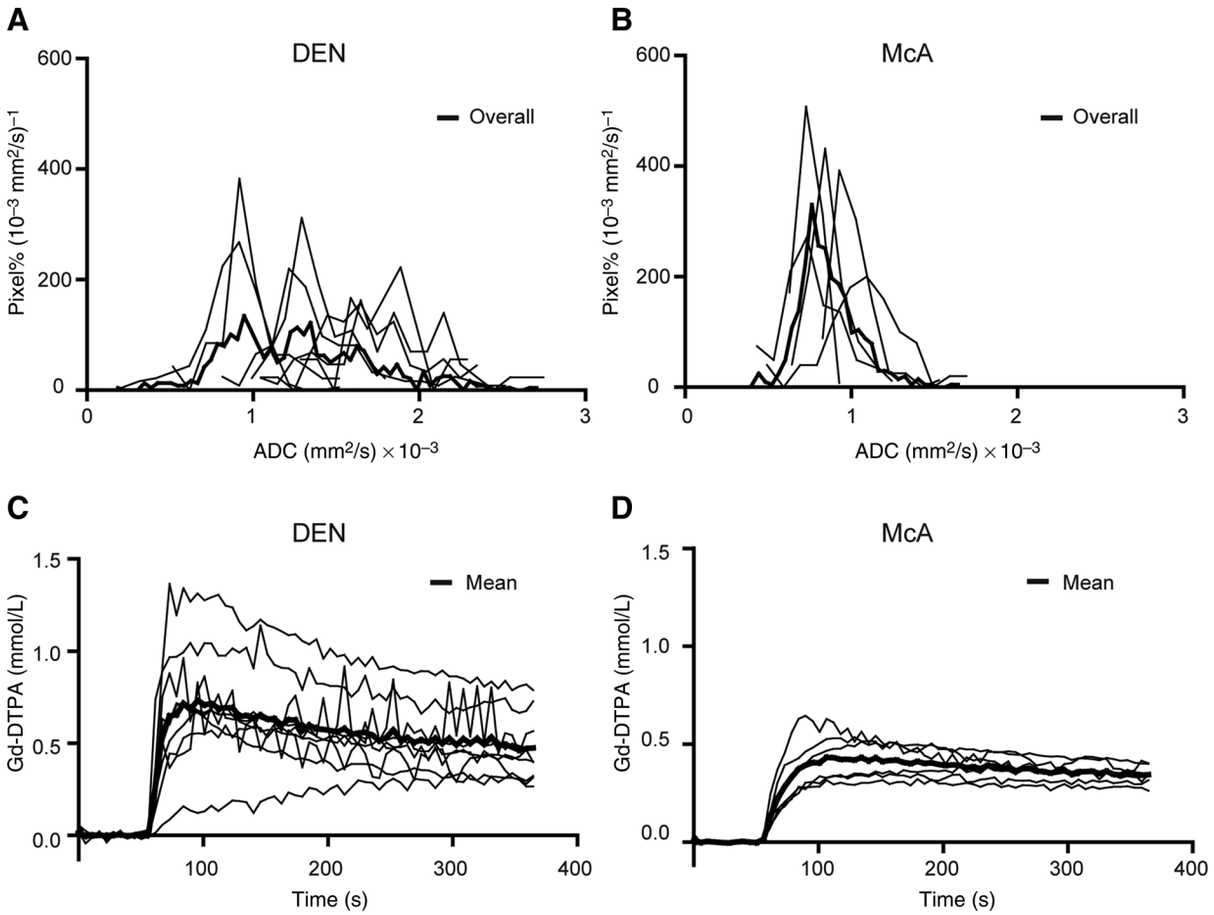

Figure 3.
Heterogeneity of DEN and McA tumor populations as determined by MRI analyses. A and B, normalized individual (thin) and mean (bold) ADC histographs of DEN and McA tumors show broader voxel distribution in DEN tumors, reflecting a higher level of tissue heterogeneity. Mean ADC value of DEN: 1.48 ± 0.37; mean ADC value of McA: 0.97 ± 0.15. C and D, individual (thin) and mean (bold) Gd-DTPA concentration time curves of DEN and McA tumors show steeper initial slopes, higher peak values, and more interindividual variability in DEN tumors.

with the Ki-67 staining index (24 ± 13 and 57 ± 7%) in DEN and McA tumors, respectively (Fig. 2C). In agreement with tumor grading and proliferation rate, DEN tumors exhibited lower FDG uptake compared with McA tumors (4.8 ± 1.5 and 9.7 ± 3.2, $P < 0.0001$; Fig. 2D). Tumor proliferation was also assessed by FLT-PET; however, uptake was overall low and no significant difference was detected between the two model systems (1.2 ± 0.2 and 1.3 ± 0.2).

Heterogeneity was further confirmed by array comparative genomic hybridization (aCGH) analyses. aCGH revealed chromosomal aberrations in all HCCs (Fig. 2E and F). Whereas orthotopically implanted (McA) rat HCCs were characterized by a large number of chromosomal aberrations, DEN-induced tumors displayed only a few aberrations. Moreover, for the McA tumors a recurrent aberration pattern could be found. This was supported by the principal component analysis (PCA) of aCGH data (Supplementary Fig. S3A), demonstrating more pronounced similarity within the group of McA tumors compared with the more heterogeneous group of DEN-induced HCCs. In addition, hierarchical cluster analysis revealed intraindividual heterogeneity, suggestive of multifocal tumor development in DEN animals (data not shown). Furthermore, we compared genomic copy-number alterations detected in our rat models with that from a human set of cryptogenic HCCs using synteny information and found good concordance (Supplementary Fig. S3B–S3E).

Figure 2.
Histopathologic tumor grading and tumor growth kinetics. A, histopathologic tumor grading reveals differential grading in DEN animals only (DEN: G1 $n = 1$, G2 $n = 6$, G3 $n = 7$; McA: G3 $n = 8$). B, tumor growth curves show a faster and more homogeneous growth pattern of McA tumors. C, semiquantitative analysis of Ki-67 antibody staining reveals a higher percentage of positive staining in McA tumors; mean values ±SEM and P values are shown. D, quantitative analysis of FDG uptake reveals higher tumor to muscle ratios of McA compared with DEN animals. E and F, 32 samples of DEN induced ($n = 20$; E) and orthotopically implanted McA ($n = 12$; F) rat HCCs. Chromosomes 1 to 20 are shown from p- to q-arm, and dark horizontal bars within the symbolized chromosomes represent G bands. Chromosomal gains and losses are indicated in black and gray, respectively.

Published OnlineFirst May 20, 2015; DOI: 10.1158/1078-0432.CCR-14-2018

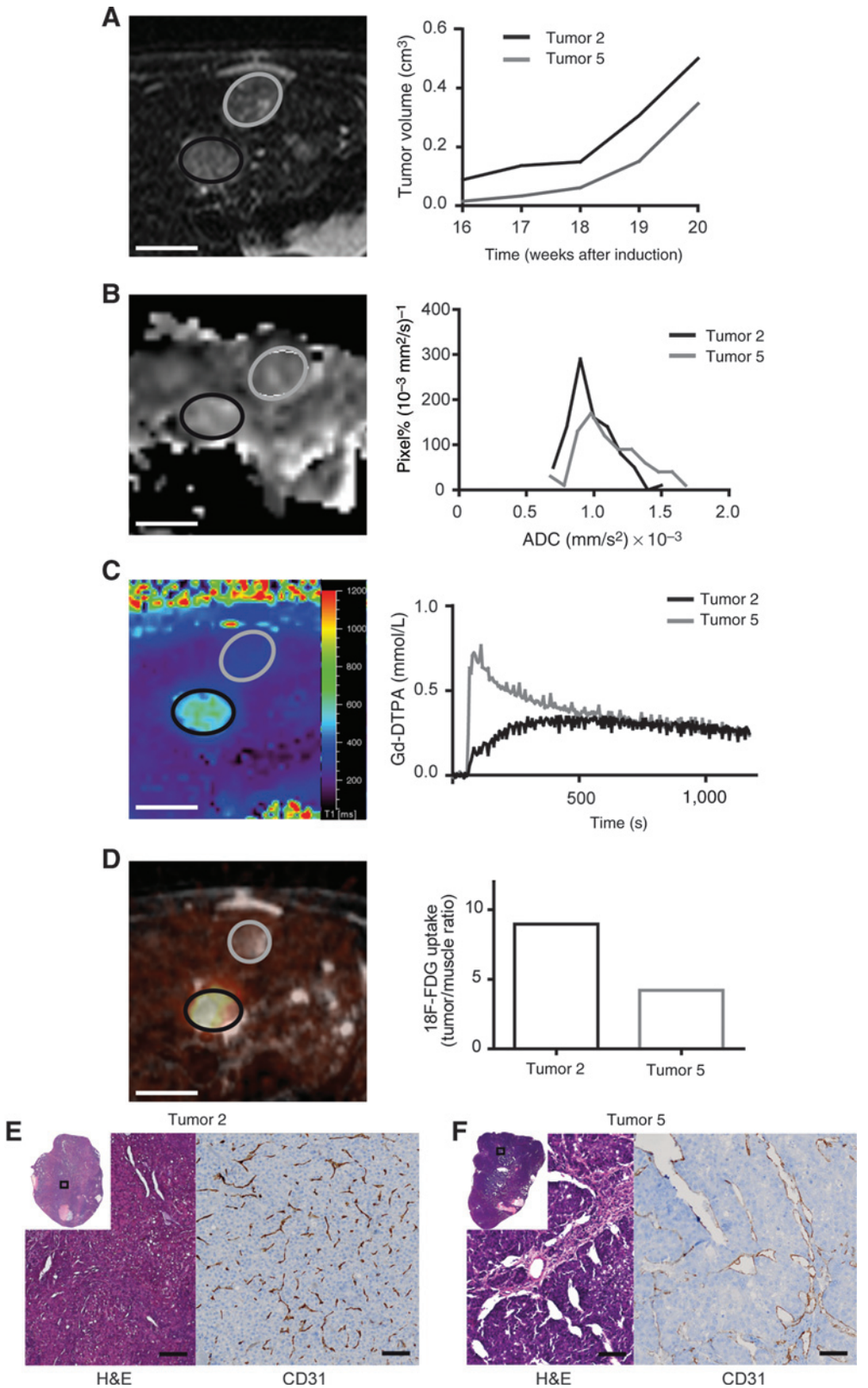

Published OnlineFirst May 20, 2015; DOI: 10.1158/1078-0432.CCR-14-2018

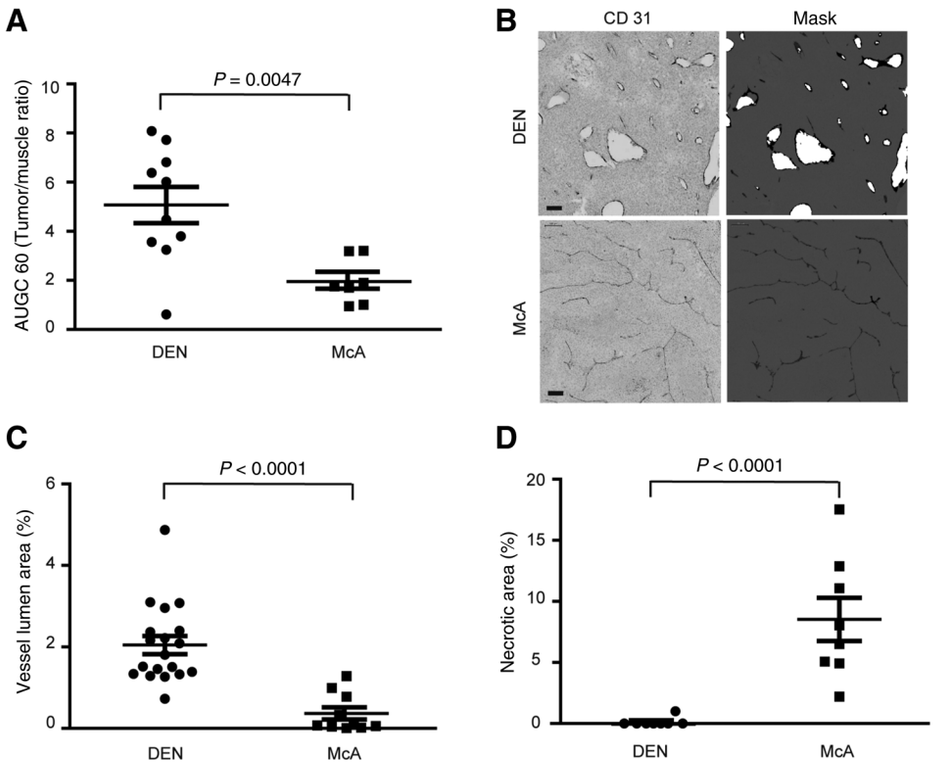

Figure 5.
Tumor vascularization. A, normalized tumor AUGC60 values are significantly higher in DEN compared with McA tumors. B, representative photomicrographs of CD31 antibody stained center tumor slices (left) and respective masks used for semiautomated vessel lumen segmentation (right) of DEN (top) and McA (bottom) tumors; scale bar, 100 μm. C, semiquantitative analysis of the relative vessel lumen of DEN and McA tumors reveals significantly higher values for DEN tumors. D, semiquantitative analysis of the relative necrosis area in DEN and McA tumors revealed a higher amount of necrosis in McA tumors; mean ± SEM and *P* values are displayed.

Inter- and intraindividual tumor tissue heterogeneity

Quantitative diffusion weighted imaging revealed broader ADC histogram distribution (Fig. 3A and B) and higher mean ADC values of DEN compared with McA tumors (1.42 ± 0.15 and 0.89 ± 0.05, $P = 0.0091$), reflecting the more heterogeneous tumor tissue composition with cystic and blood pool areas. Likewise, qualitative assessment of tumor perfusion revealed a more variable peak enhancement and shape of the Gd-DTPA concentration time curves (Fig. 3C and D) of DEN tumors compared with McA tumors. In addition, the DEN model displayed striking intertumoral heterogeneity within the same animal. This finding is exemplified in Fig. 4. Longitudinal T2w imaging (Fig. 4A) revealed no apparent differences in signal intensity or growth kinetics of the two nodules. In contrast, DWI and calculated ADC values (mean tumor 2 = 0.97 ± 0.16, tumor 5 = 1.11 ± 0.23; Fig. 4B), perfusion imaging and AUGC60 concentration time curves (Fig. 4C) and FDG PET imaging and uptake values (8.98 and 4.21; Fig. 4D), however, differed significantly. H&E and CD31 staining (Fig. 4E and F) classified tumor 2 (black line) as G3 and tumor 5 (gray line) as G2 HCC.

Response to antiangiogenic treatment

The detected differences in tumor perfusion were of particular interest because of its role in current treatment regimen based on antiangiogenic agents or TACE. AUGC60 ratios were higher in DEN animals compared with McA animals (5.07 ± 2.34 and 1.96 ± 0.92, $P = 0.0047$; Fig. 5A). This difference was also evident in quantitative histologic analyses of CD31 expression, which revealed a significantly larger mean vascular lumen area in DEN compared with McA tumors (2.05% ± 0.22 vs. 0.37% ± 0.15, $P < 0.0001$; Fig. 5B and C). The detected difference in vascularity was accompanied by less spontaneous necrosis in DEN compared with McA tumors (0.13% ± 0.35 vs. 8.53% ± 5.01, $P < 0.0001$; Fig. 5D). No differences were noted with regard to caspase-3 expression (data not shown). To further test the physiologic significance of this finding with regard to vascular targeting therapies, DEN ($n = 12$) and McA ($n = 4$) tumor-bearing animals were subjected to sorafenib treatment. Interestingly, DEN tumors only showed reduced AUGC60 ratios (Fig. 6A) and tumor volume growth kinetics in the treatment compared with the placebo group (Fig. 6C), whereas sorafenib treatment induced no change in McA tumors (Fig. 6B and D). The copy-number status of the *Vegfr* and

Figure 4.
Intraindividual tumor heterogeneity. A, T2w image; B, ADC map; C, T1 map of time point t12 (72s) with color scale indicating different T1 values in ms and (D) T2w/FDG fusion image displaying the same two tumor nodules within one DEN animal (Tu2 = black circle; Tu5 = gray circle). A, Tumor volume curves of Tu2 and Tu5 between weeks 16 and 20 reveal an earlier onset of Tu2 compared with Tu5 but similar growth kinetics; scale bar, 1 cm. B, ADC histograms show lower mean values for Tu2 compared with Tu5 (Tu2 = 0.97 ± 0.16, Tu5 = 1.11 ± 0.23); scale bar, 1 cm. C, Gd-DTPA concentration time curves indicate major differences in tumor perfusion, with a faster wash-in and wash-out in Tu5; scale bar, 1 cm. D, FDG-imaging shows higher FDG tracer uptake in Tu2 (8.98 vs. 4.21); scale bar, 1 cm. E and F, photomicrographs of H&E and CD31 antibody staining show the dense tissue architecture (E, left) with closed microvessels (E, right) of Tu2 and the loose tissue architecture with fibrosis (F, left) and open microvessels (F, right) of Tu5; scale bar, 100 μm.

Published OnlineFirst May 20, 2015; DOI: 10.1158/1078-0432.CCR-14-2018

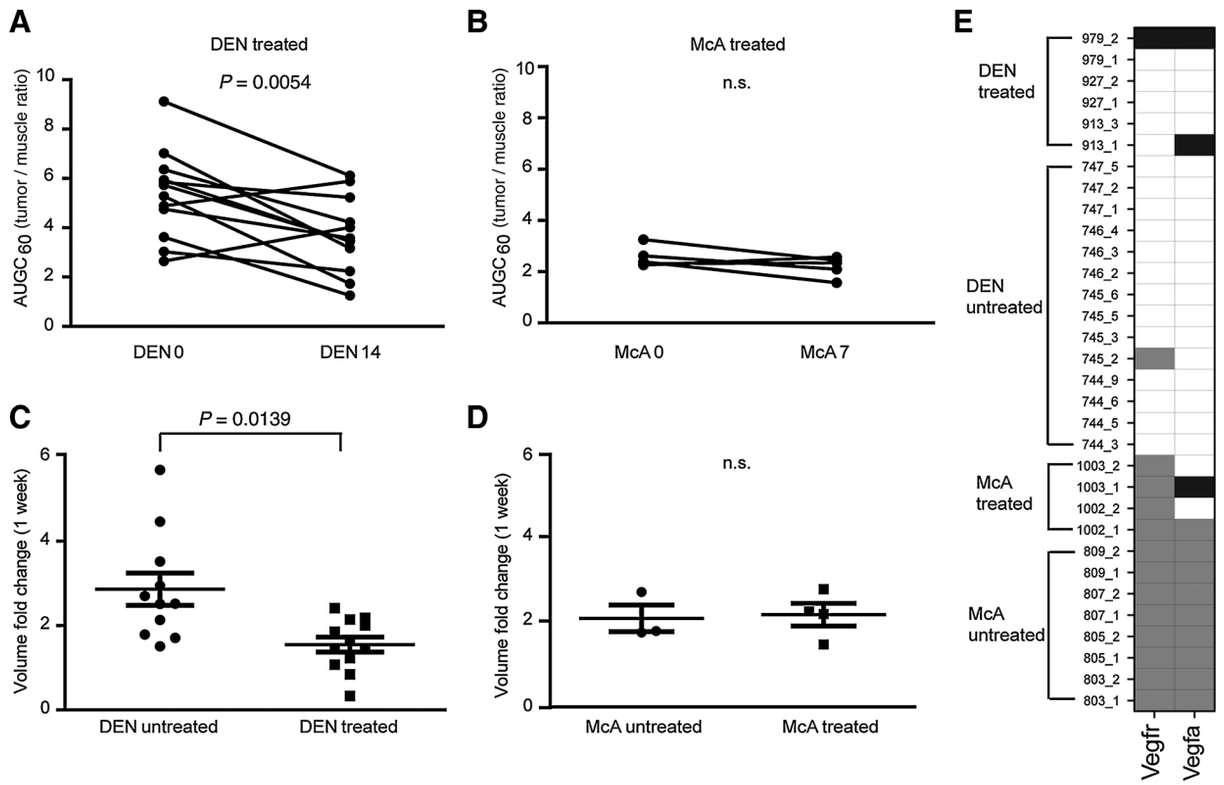

Figure 6.
Semiquantitative perfusion and volume analysis after antiangiogenic treatment. A and B, AUGC60 values before (day 0) and after therapy (days 7 and 14) reveal a significant decrease in DEN and no change in McA tumors. C and D, accordingly, only DEN tumors showed reduced volume growth kinetics. E, the copy-number status of the genes Vegfr and Vegfa is shown for all HCCs samples analyzed. Chromosomal amplifications and deletions are indicated in black and gray, respectively.

Vegfa genes showed amplifications of both genes in the McA model predominantly, independent of the treatment status (Fig. 6E).

Discussion

In this work, we compared transplanted (McA) and chemically induced (DEN) rat HCC by multimodal, multiparametric imaging, to identify differences in tumor biology and to analyze tumor response to the only clinically approved systemic antiangiogenic agent sorafenib. All analyzed imaging parameters, including volume growth kinetics, calculated ADC values, AUGC60 values and FDG uptake exhibited differences between the two model systems. Furthermore, greater inter- and intraindividual tumor heterogeneity was seen in the DEN model. Sorafenib treatment resulted in reduced AUGC60 values and volume growth kinetics and increased necrosis in the DEN model and had no apparent effect in the McA model.

Choice of model system

Animal models play a crucial role in research on HCC with a wide variety of model systems at hand. Most often, mouse models have been favored because of the wealth of species-specific molecular and genetic tools available. However, imaging and intervention (e.g., TACE procedures), of particular interest in translational studies on HCC, are difficult to realize in mice due to size restrictions (20, 7, 21). We chose the DEN model because of its genetic similarity to human HCC (22). Furthermore, previous reports described the development of HCC in DEN fed animals within a chronically damaged liver background, similar to the human scenario (23). On the other hand, orthotopically transplanted rat HCC is considered a valuable time- and cost-efficient model system, widely used in preclinical drug efficacy studies (24, 25). The differences in tumor physiology detected between the two models likely reflect a mixture of local (i.e., tumoral) and systemic (i.e., strain) physiology. A comparison of genomic copy-number alterations detected in the applied animal models with that occurring in a human array CGH dataset on cryptogenic HCCs (Supplementary Fig. S3B–S3E; ref. 18) by synteny analysis showed the majority of copy number alterations present in both datasets.

Liver damage

Biochemical liver function tests and histologic analyses confirm previous reports of a chronic toxic liver damage in the DEN model system. Tissue damage was classified as mild to moderate fibrosis rather than cirrhosis. Furthermore, increased FDG uptake, increased hepatocyte proliferation and the presence of inflammatory cells also indicated an earlier stage of chronic liver damage compared with previous reports. Increased liver to muscle AUGC60 values in addition suggest an proangiogenic response as recently reported in the CCl4 and bile duct ligation models (26). Similarly, an arterialization of the regular sinusoidal blood supply is described for progressive liver disease in precirrhotic human subjects (27). The confirmation of chronic liver damage in the DEN model has important implications with regard to

Published OnlineFirst May 20, 2015; DOI: 10.1158/1078-0432.CCR-14-2018

imaging as well as drug efficacy studies. First, sensitivity and specificity, and thus the value of a particular imaging technique depend on the tumor-to-background contrast that can be achieved with the particular technique. Especially in heterotopic model systems these are often artificially high (e.g., subcutaneous tumor implants). Second, a compromised liver function presents a major obstacle in clinical therapy trials, which are often jeopardized by increased drug toxicity (28).

Tumor heterogeneity

In our study, we noted a large amount of intra- and intertumoral variability in the DEN model. Tumor heterogeneity is a characteristic feature of several cancer types, including HCC (29, 30). It presents a significant barrier to effective therapy development, and thus is of particular importance in preclinical drug efficacy studies. Quantitative assessment of this heterogeneity in HCC physiology by noninvasive imaging has been proposed (31, 32), but presents a major challenge in clinical routine, due to motion artifacts and insufficient spatial resolution in abdominal imaging. Several studies are now beginning to address this issue with documented intra- and intersubject variability in several biomarkers, including FDG uptake, as well as DWI- and DCE-MRI parameters (33, 34). The DEN model, therefore, may present a valuable tool, representing the complexity of the human disease, enabling the validation of imaging markers that identify subtypes and their testing in future co-clinical trials.

Tumor perfusion and sorafenib response

AUGC60 and CD31 staining revealed higher mean values and more variability in DEN compared with McA tumors; preliminary histopathologic analyses of human HCC specimen ($n = 7$) showed CD34 staining and necrosis levels more similar to those found in the DEN model (lumen area $1.17\% \pm 0.15$, $P = 0.03$; necrosis: $0.64\% \pm 0.42$; Supplementary Fig. S4). These differences in perfusion related parameters are of particular importance for several reasons. A high level of tumor perfusion provides the rationale for antiangiogenic and TACE treatment in human HCC, and thus should be reflected in a preclinical model system. Furthermore, variability in tumor perfusion has also been described for human HCC, where it correlates with tumor grading, thus presenting a potential biomarker of histopathologic grading (35). Considering the potential of metabolic imaging in tumor characterization and response monitoring, for example, by FDG-PET or hyperpolarized 13C metabolite magnetic resonance spectroscopy imaging, quantitative assessment of tumor perfusion may aid in the validation of such imaging markers.

We can only speculate with regard to the underlying cause of the differences in vascularity between DEN and McA tumors. Mechanical stress from increased intratumoral pressure, resulting in vessel compression may in part explain the observed difference (36). Furthermore, lower perfusion values in McA tumors may indicate a vascular supply similar to that of liver metastases rather than HCC (12). Also growth kinetics in McA tumors on average, are higher compared with DEN tumors possibly related to a less mature vascular phenotype in McA tumors.

We still have a limited understanding of the mechanism of action of sorafenib in advanced stage HCC. Sorafenib targets tyrosine kinases, including BRAF, the vascular endothelial growth factor receptor (VEGFR), and platelet-derived growth factor receptor (PDGFR), and thus inhibit multiple kinases that may be active in HCC. In the DEN model, 20% of the tumor nodules exhibit BRAF point mutations (37). Accordingly, the effects seen on tumor perfusion and growth kinetics in DEN tumors are not easily dissected and may be attributable to tumor cell toxicity and antiangiogenic action.

Pikarsky's group recently identified a VEGF-based paracrine activation loop between tumor cells and tumor macrophages (38). Despite *Vegfa* amplification in McA tumors, blockage thereof failed to control tumor growth, possibly due to the lack of macrophage recruitment in this model system as shown immunohistochemically (Supplementary Fig. S2A).

Limitations

Different rat strains were used in the DEN and McA model, presenting a potential limitation. However, differences in tumor perfusion were confirmed by histologic findings. Sorafenib treatment in the McA model was limited to 1 week, and had to be discontinued due to rapid tumor progression. A longer treatment course or an earlier start may have resulted in therapy response in the McA model as well. Furthermore, only a small number of human samples were analyzed for vascular staining and no correlation with perfusion values has been performed so far.

Our study quantifies differences in tumor physiology between DEN and McA tumors, underlining the importance of preclinical model selection. Of particular interest are the significantly higher tumor perfusion values and tumor heterogeneity found in the DEN model. The detected heterogeneity in DEN tumors may provide an opportunity for further investigation of HCC subtypes and respective biomarkers.

Disclosure of Potential Conflicts of Interest

No potential conflicts of interest were disclosed.

Authors' Contributions

Conception and design: C. Groß, S. Sayyed, O. Ebert, M. Schwaiger, E. Rummeny, A. Steingötter, R. Braren

Development of methodology: C. Groß, S. Sayyed, I. Heid, A. Feuchtinger, A. Walch, J. Altomonte, M. Schwaiger, A. Steingötter, I. Esposito, R. Braren

Acquisition of data (provided animals, acquired and managed patients, provided facilities, etc.): C. Groß, S. Sayyed, I. Heid, A. Feuchtinger, A. Walch, J. Heß, K. Unger, J. Dworniczak

Analysis and interpretation of data (e.g., statistical analysis, biostatistics, computational analysis): C. Groß, K. Steiger, S. Sayyed, I. Heid, A. Feuchtinger, A. Walch, J. Heß, K. Unger, H. Zitzelsberger, A.M. Schlitter, J. Dworniczak, E. Rummeny, I. Esposito, R. Braren

Writing, review, and/or revision of the manuscript: C. Groß, I. Heid, J. Heß, K. Unger, J. Altomonte, O. Ebert, M. Schwaiger, E. Rummeny, A. Steingötter, I. Esposito, R. Braren

Administrative, technical, or material support (i.e., reporting or organizing data, constructing databases): C. Groß, I. Heid, M. Settles, J. Dworniczak, J. Altomonte, M. Schwaiger

Study supervision: H. Zitzelsberger, E. Rummeny, R. Braren

Acknowledgments

The authors thank Yvonne Kosanke, Sybille Reder, and Iryna Skuratovska for excellent technical assistance.

Grant Support

This work was supported by the German Research Foundation (DFG) within the SFB-Initiative 824 (collaborative research center), "Imaging for Selection, Monitoring, and Individualization of Cancer Therapies" (SFB824, projects C6, Z2).

The costs of publication of this article were defrayed in part by the payment of page charges. This article must therefore be hereby marked *advertisement* in accordance with 18 U.S.C. Section 1734 solely to indicate this fact.

Received August 11, 2014; revised April 15, 2015; accepted May 8, 2015; published OnlineFirst May 20, 2015.

Published OnlineFirst May 20, 2015; DOI: 10.1158/1078-0432.CCR-14-2018

References

1. Ferlay J, Shin HR, Bray F, Forman D, Mathers C, Parkin DM. Estimates of worldwide burden of cancer in 2008: GLOBOCAN 2008. Int J Cancer 2010;127:2893–917.
2. Hayashi M, Matsui O, Ueda K, Kawamori Y, Gabata T, Kadoya M. Progression to hypervascular hepatocellular carcinoma: correlation with intranodular blood supply evaluated with CT during intraarterial injection of contrast material. Radiology 2002;225:143–9.
3. Braren R, Curcic J, Remmele S, Altomonte J, Ebert O, Rummeny EJ, et al. Free-breathing quantitative dynamic contrast-enhanced magnetic resonance imaging in a rat liver tumor model using dynamic radial T(1) mapping. Invest Radiol 2011;46:624–31.
4. Lencioni R, Llovet JM. Modified RECIST (mRECIST) assessment for hepatocellular carcinoma. Semin Liver Dis 2010;30:52–60.
5. Zhu AX, Duda DG, Sahani DV, Jain RK. HCC and angiogenesis: possible targets and future directions. Nat Rev Clin Oncol 2011;8:292–301.
6. Landis CS, Li X, Telang FW, Coderre JA, Micca PL, Rooney WD, et al. Determination of the MRI contrast agent concentration time course *in vivo* following bolus injection: effect of equilibrium transcytolemmal water exchange. Magn Reson Med 2000;44:563–74.
7. Newell P, Villanueva A, Friedman SL, Koike K, Llovet JM. Experimental models of hepatocellular carcinoma. J Hepatol 2008;48:858–79.
8. Wilhelm SM, Adnane L, Newell P, Villanueva A, Llovet JM, Lynch M. Preclinical overview of sorafenib, a multikinase inhibitor that targets both Raf and VEGF and PDGF receptor tyrosine kinase signaling. Mol Cancer Ther 2008;7:3129–40.
9. Llovet JM, Ricci S, Mazzaferro V, Hilgard P, Gane E, Blanc JF, et al. Sorafenib in advanced hepatocellular carcinoma. N Engl J Med 2008; 359:378–90.
10. Braren R, Altomonte J, Settles M, Neff F, Esposito I, Ebert O, et al. Validation of preclinical multiparametric imaging for prediction of necrosis in hepatocellular carcinoma after embolization. J Hepatol 2011;55:1034–40.
11. Altomonte J, Braren R, Schulz S, Marozin S, Rummeny EJ, Schmid RM, et al. Synergistic antitumor effects of transarterial viroembolization for multifocal hepatocellular carcinoma in rats. Hepatology 2008;48:1864–73.
12. Abdullah SS, Pialat JB, Wiart M, Duboeuf F, Mabrut JY, Bancel B, et al. Characterization of hepatocellular carcinoma and colorectal liver metastasis by means of perfusion MRI. J Magn Reson Imaging 2008;28:390–5.
13. Aaltonen LA, Hamilton SRWorld Health Organization, International Agency for Research on Cancer. Pathology and genetics of tumours of the digestive system. Lyon Oxford: IARC Press; Oxford University Press (distributor); 2000. 314 p. p.
14. Thoolen B, Maronpot RR, Harada T, Nyska A, Rousseaux C, Nolte T, et al. Proliferative and nonproliferative lesions of the rat and mouse hepatobiliary system. Toxicol Pathol 2010;38(7 Suppl):5S–81S.
15. Neuvial P, Hupe P, Brito I, Liva S, Manie E, Brennetot C, et al. Spatial normalization of array-CGH data. BMC Bioinformatics 2006;7:264.
16. van de Wiel MA, Kim KI, Vosse SJ, van Wieringen WN, Wilting SM, Ylstra B. CGHcall: calling aberrations for array CGH tumor profiles. Bioinformatics 2007;23:892–4.
17. van de Wiel MA, Wieringen WN. CGHregions: dimension reduction for array CGH data with minimal information loss. Cancer Inform 2007;3: 55–63.
18. Schlaeger C, Longerich T, Schiller C, Bewerunge P, Mehrabi A, Toedt G, et al. Etiology-dependent molecular mechanisms in human hepatocarcinogenesis. Hepatology 2008;47:511–20.
19. Wolf MJ, Adili A, Piotrowitz K, Abdullah Z, Boege Y, Stemmer K, et al. Metabolic activation of intrahepatic $CD8^+$ T cells and NKT cells causes nonalcoholic steatohepatitis and liver cancer via cross-talk with hepatocytes. Cancer Cell 2014;26:549–64.
20. Heindryckx F, Colle I, Van Vlierberghe H. Experimental mouse models for hepatocellular carcinoma research. Int J Exp Pathol 2009;90:367–86.
21. Wu L, Tang ZY, Li Y. Experimental models of hepatocellular carcinoma: developments and evolution. J Cancer Res Clin Oncol 2009;135:969–81.
22. Lee JS, Thorgeirsson SS. Comparative and integrative functional genomics of HCC. Oncogene 2006;25:3801–9.
23. Polasek M, Fuchs BC, Uppal R, Schuhle DT, Alford JK, Loving GS, et al. Molecular MR imaging of liver fibrosis: a feasibility study using rat and mouse models. J Hepatol 2012;57:549–55.
24. Cho HR, Choi JW, Kim HC, Song YS, Kim GM, Son KR, et al. Sprague-Dawley rats bearing McA-RH7777 cells for study of hepatoma and transarterial chemoembolization. Anticancer Res 2013;33:223–30.
25. Choi JW, Kim H, Kim HC, Lee Y, Kwon J, Yoo RE, et al. Blood oxygen level-dependent MRI for evaluation of early response of liver tumors to chemoembolization: an animal study. Anticancer Res 2013;33:1887–92.
26. Ehling J, Bartneck M, Wei X, Gremse F, Fech V, Mockel D, et al. CCL2-dependent infiltrating macrophages promote angiogenesis in progressive liver fibrosis. Gut 2014;63:1960–71.
27. Coulon S, Heindryckx F, Geerts A, Van Steenkiste C, Colle I, Van Vlierberghe H. Angiogenesis in chronic liver disease and its complications. Liver Int 2011;31:146–62.
28. Worns MA, Galle PR. HCC therapies-lessons learned. Nat Rev Gastroenterol Hepatol 2014;11:447–52.
29. Hoshida Y, Nijman SM, Kobayashi M, Chan JA, Brunet JP, Chiang DY, et al. Integrative transcriptome analysis reveals common molecular subclasses of human hepatocellular carcinoma. Cancer Res 2009;69:7385–92.
30. Hoshida Y, Villanueva A, Kobayashi M, Peix J, Chiang DY, Camargo A, et al. Gene expression in fixed tissues and outcome in hepatocellular carcinoma. N Engl J Med 2008;359:1995–2004.
31. Rutman AM, Kuo MD. Radiogenomics: creating a link between molecular diagnostics and diagnostic imaging. Eur J Radiol 2009;70:232–41.
32. Segal E, Sirlin CB, Ooi C, Adler AS, Gollub J, Chen X, et al. Decoding global gene expression programs in liver cancer by noninvasive imaging. Nat Biotechnol 2007;25:675–80.
33. Dong A, Yu H, Wang Y, Dong H, Zuo C. FDG PET/CT and enhanced CT imaging of tumor heterogeneity in hepatocellular carcinoma: imaging-pathologic correlation. Clin Nucl Med 2014;39:808–10.
34. Kim KA, Park MS, Ji HJ, Park JY, Han KH, Kim MJ, et al. Diffusion and perfusion MRI prediction of progression-free survival in patients with hepatocellular carcinoma treated with concurrent chemoradiotherapy. J Magn Reson Imaging 2014;39:286–92.
35. Lee JH, Lee JM, Kim SJ, Baek JH, Yun SH, Kim KW, et al. Enhancement patterns of hepatocellular carcinomas on multiphasicmultidetector row CT: comparison with pathological differentiation. Br J Radiol 2012;85: e573–83.
36. Stylianopoulos T, Martin JD, Chauhan VP, Jain SR, Diop-Frimpong B, Bardeesy N, et al. Causes, consequences, and remedies for growth-induced solid stress in murine and human tumors. Proc Natl Acad Sci U S A 109:15101–8.
37. Jaworski M, Ittrich C, Hailfinger S, Bonin M, Buchmann A, Schwarz M, et al. Global gene expression in Ha-ras and B-raf mutated mouse liver tumors. Int J Cancer 2007;121:1382–5.
38. Horwitz E, Stein I, Andreozzi M, Nemeth J, Shoham A, Pappo O, et al. Human and mouse VEGFA-amplified hepatocellular carcinomas are highly sensitive to sorafenib treatment. Cancer Discov 2014;4:730–43.